

The maximum mass and rotational kinetic energy of rapidly rotating neutron stars

Shao-Peng Tang,¹ Yong-Jia Huang,^{1,2} and Yi-Zhong Fan^{1,3,*}

¹Key Laboratory of Dark Matter and Space Astronomy,

Purple Mountain Observatory, Chinese Academy of Sciences, Nanjing 210033, China

²RIKEN Interdisciplinary Theoretical and Mathematical Sciences Program (iTHEMS), RIKEN, Wako 351-0198, Japan

³School of Astronomy and Space Science, University of Science and Technology of China, Hefei, Anhui 230026, China

(Dated: May 1, 2025)

Rapid uniformly-rotating neutron stars are expected to be formed for instance in the collapse of some massive stars, the accretion of some compact object binaries, and some double neutron star mergers. The huge amount of the rotational energy has been widely believed to be the source of some cosmic gamma-ray bursts and superluminous supernovae. Benefited from the tight constraints on the equation of state of the neutron star matter set by the latest multi-messenger data, the chiral effective field theory (χ EFT) and perturbative quantum chromodynamics (pQCD), here we present the maximum gravitational mass as well as the kinetic rotational energy for a neutron star at a given spin period. Our nonparametric EOS analysis reveals that the critical Keplerian configurations ($\Omega_{\text{kep}}^{\text{crit}} = 1.00 \pm 0.07 \times 10^4$ rad/s) can sustain maximum gravitational masses of $M_{\text{kep}}^{\text{crit}} = 2.76_{-0.09}^{+0.11} M_{\odot}$ with corresponding rotational energy reaching $E_{\text{rot,kep}}^{\text{crit}} = 2.38_{-0.24}^{+0.25} \times 10^{53}$. However, the maximum rotational energy that can be feasibly extracted from a neutron star is limited to $1.40_{-0.13}^{+0.15} \times 10^{53}$ erg, which holds for a baryon mass of $2.68_{-0.09}^{+0.10} M_{\odot}$. All these parameters, obtained via the nonparametric reconstruction of the equation of state, are at the 68.3% confidence level and the adoption of a quarkonic model yields rather similar results. These findings are found to have already set some intriguing constraints on the millisecond magnetar interpretation of some exciting data.

I. INTRODUCTION

In the universe, there are various kinds of very energetic outbursts such as gamma-ray bursts and superluminous supernovae. Though the black hole central engine has been widely adopted to interpret these phenomena, the rapidly rotating magnetized neutron star model can well account for some observational facts [1–8] and has also attracted wide attention. One particularly interesting scenario is the merger of the double neutron stars, in which the formed massive remnant, if not collapsed into black hole quickly, will rotate at the mass shedding limit [9, 10]. Very rapid rotation of the newly formed neutron star is also expected if the progenitor massive star has a high angular momentum [11]. A fundamental question is hence how large the rotational kinetic energy of the extremely spinning neutron star could be. In principle, this energy reservoir governs the violence of the energetic explosions as well as the capability of accelerating the ultra-high energy cosmic rays. The other relevant question is what the upper bound on the allowed gravitational mass in the case of rapid uniform rotation. It plays an essential role in revealing the nature of the $\sim 2.4 - 3M_{\odot}$ mysterious compact objects detected in the Galaxy [12] and by the gravitational wave detectors [13, 14]. Certainly, it is not possible to answer these two intriguing questions analytically. The main purpose of this work is to reliably evaluate them numerically, benefiting from the recent breakthroughs on neutron star mass and radius measurements as well as the theoretical advancements. For instance, the NICER mission has recently extended its measurements by determining the radius of PSR J0437–4715 [15], complementing earlier mass–radius determinations for PSR J0030+0451 [16] and PSR J0740+6620 [17, 18]. These data, together with gravitational-wave event GW170817 [19, 20], we now have five neutron stars with reasonably measured mass and radius. On the theoretical frontier, the chiral effective field theory (χ EFT) can robustly describe the equation of state up to the nuclear saturation density [21], while perturbative QCD calculations have emerged as a valuable tool for constraining the very high-density behavior of nuclear matter [22–24]. The measurements of the masses of about 100 neutron stars provide a mass distribution function that can be used to constrain M_{TOV} , the maximum gravitational mass of nonrotating neutron stars [25–27]. Previously, the combination of these data and theoretical information has already yielded tight constraints on the equation of state of the dense neutron star matter and hence the accurate inference of $M_{\text{TOV}} = 2.25_{-0.07}^{+0.08} M_{\odot}$ [27–29]. Interestingly, such a maximum mass already seems to be challenged by the indirectly-measured gravitational mass $2.35 \pm 0.17 M_{\odot}$ of PSR J0952–0607 [30]. This puzzle may be resolved, as the rapid rotation of PSR J0952–0607 could effectively enhance its gravitational mass [31, 32]. Motivated by the above facts, in this work we examine the effect of rapid uniform rotation, which is widely adopted in interpreting observational

* Corresponding author. yzfan@pmo.ac.cn

data in the literature. Before carrying out the numerical calculations with the RNS code [31], we reconstruct the equation of state of the neutron star matter in two ways, one is the nonparametric Gaussian Process-based model and the other is a quarkyonic model. For the equation of state of neutron star matter that matches current observational data and physical information, we derive the range of critical collapse masses as a function of rotation period and, concurrently, the corresponding range of maximum rotational energy and maximum extractable energy. Our main finding includes the maximum angular velocity of $1.00 \pm 0.07 \times 10^4$ (rad/s), the rotational kinetic energy bound of $2.38_{-0.24}^{+0.25} \times 10^{53}$ erg, the maximum extractable energy bound of $1.40_{-0.13}^{+0.15} \times 10^{53}$ erg, and the gravitational mass upper limit of $2.76_{-0.09}^{+0.11} M_{\odot}$, for rapid uniformly-rotating neutron stars. These thresholds are expected to be very helpful in better understanding some astrophysical phenomena.

II. METHODS

Previous studies employing nonparametric approaches—including the single-layer feed-forward neural network [24], the piecewise linear sound speed model [33], and Gaussian process (GP) method [34–36]—have produced very consistent EOS reconstruction results [27]. In this work, we adopt the GP method as our primary tool for constructing the neutron star EOS, which allows for a flexible, smooth extension from the low-density regime into the high-density domain while avoiding the limitations of fixed parametric forms (for further details, see Refs. [23, 37]).

In addition to this flexible, phenomenological GP model, we implement a physically motivated parameterized EOS model, the quarkyonic model [38, 39], which offers microscopic insight into high-density matter and naturally explains the stiffening of the EOS. In the quarkyonic model, as the baryon density exceeds a threshold n_t , nucleons become confined to a narrow shell in momentum space near the Fermi surface while free quarks populate the lower momentum states. This coexistence of a free quark Fermi sea with nucleons contributes extra kinetic pressure, resulting in a rapid increase in pressure and a peak in the speed of sound. In the formulation of Ref. [40], an explicit momentum cutoff is imposed on nucleons. In practice, the minimum momentum for neutrons (or protons) is parameterized as

$$k_{0(n,p)} = k_{F(n,p)} \left[1 - \left(\frac{\Lambda}{k_{F(n,p)}} \right)^{\alpha} - \frac{\kappa_{n,p} \Lambda}{9 k_{F(n,p)}} \right], \quad (1)$$

where $k_{F(n,p)}$ is the Fermi momentum of neutrons (or protons), Λ controls the width of the momentum shell, $\kappa_{n,p}$ are model parameters determined by the ambient beta-equilibrium conditions at n_t , and α (typically 2 or 3) determines the sharpness of the cutoff. This construction forces quarks to “drip” out of the nucleons, thereby increasing their kinetic energy and overall pressure. Moreover, the model is extended to include protons and leptons so that chemical and beta equilibrium are maintained. While the complete formulation involves several parameters to accurately reproduce nuclear matter properties, we here adopt a simplified ndu version from Ref. [40]. This reduced version retains the key physical ingredients—the nucleon–quark transition, momentum-space restrictions, and equilibrium conditions—while allowing for efficient, analytic EOS calculations. The prior distributions for the ndu model parameters are chosen based on physical expectations and experimental constraints. Specifically, L (the slope of symmetry energy), Λ , and n_t are uniformly distributed within ranges of (20, 100) MeV, (300, 2500) MeV, and (0.2, 0.6) fm⁻³, respectively. The nuclear saturation density, n_s , binding energy, BE, and symmetry energy parameter, S_v , are Gaussian distributed, with $n_s \sim \mathcal{N}(0.157, 0.005^2)$ fm⁻³, $\text{BE} \sim \mathcal{N}(-15.97, 0.2^2)$ MeV, and $S_v \sim \mathcal{N}(32, 0.55^2)$ MeV, respectively [41]. The PNM potential parameter γ_1 in Equation (10) of Ref. [40] is uniformly distributed, $\gamma_1 \sim \text{Uniform}(4/3, 2)$. And we employ the SLy4 [42] crust EOS for $n < 0.5n_s$.

Once the EOS is constructed by either method, we solve the Tolman–Oppenheimer–Volkoff (TOV) and Regge–Wheeler equations to generate mass–radius and mass–tidal deformability curves.

We use the latest multimessenger observations and theoretical pQCD calculations to rigorously constrain the neutron star equation of state. The key datasets incorporated into our Bayesian framework are as follows: First, the NICER X-ray timing observations provide precise radius measurements for several neutron stars, including PSR J0437–4715 with a radius of $11.36_{-0.63}^{+0.95}$ km (at the 68% credible level) [15], PSR J0030+0451 with a radius of $11.71_{-0.83}^{+0.88}$ km derived using the ST+PDT model [16] (with alternative models like PDT-U being disfavored [43]), and PSR J0740+6620 with a radius of $12.49_{-0.88}^{+1.28}$ km [17]. Second, the gravitational-wave constraints from GW170817 provide critical information on the tidal deformability of neutron stars [19, 20]. Third, we adopt the maximum mass determinations based on the marginalized posterior distribution of the maximum mass cutoff for neutron stars as reported in Ref. [27]. Finally, we apply high-density pQCD constraints at $10n_s$ [23], which, though not direct observations, provide important theoretical boundary conditions for our EOS framework.

After constraining the equation of state using observational data and theoretical constraints via both the quarkyonic and GP-based methods, the resulting EOSs are used as inputs for the RNS code [31] to compute the rotational properties of neutron stars. Specifically, we calculate sequences of uniformly rotating neutron stars at various spins

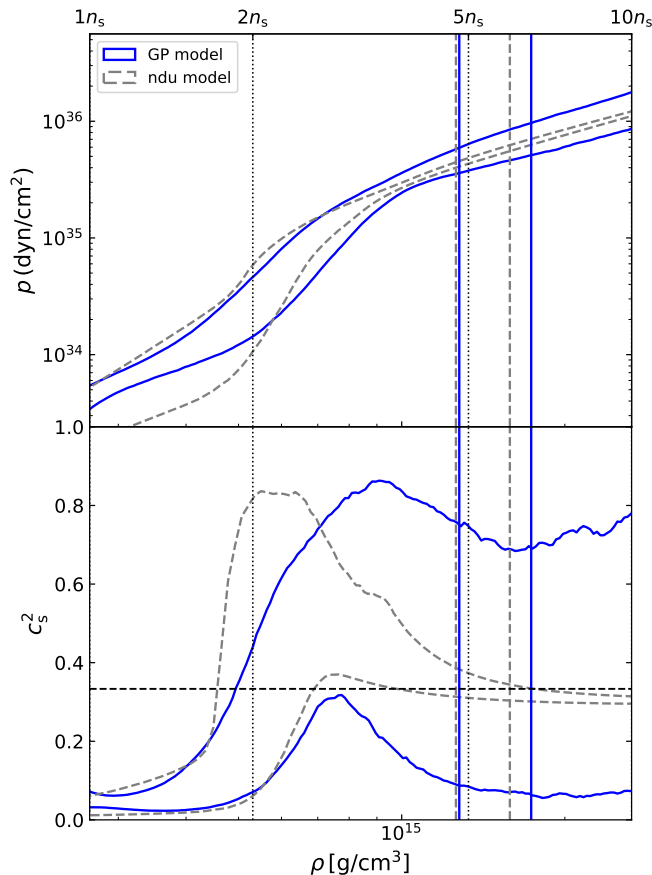


FIG. 1. The equation of states (the upper panel) and the squared sound speeds (the lower panel) reconstructed with the GP model (blue) and a specific quarkyonic model (gray) [40].

up to the mass-shedding limit for each EOS. Within these sequences, we identify the turning point along a constant-angular-momentum sequence, which marks the onset of secular instability and defines the critical configuration. At this configuration, the star is expected to collapse, and various quantities, including gravitational mass (M_{crit}), baryonic mass, radius, angular momentum, moment of inertia (I), and angular velocity (Ω), are outputted by the RNS code. We compute the rotational energy as $E_{\text{rot}} = \frac{1}{2}I\Omega^2$, and also evaluate the extractable rotational energy, E_{ext} , along constant-rest-mass sequences. For baryonic masses below the TOV limit ($M_{\text{b,TOV}}$), E_{ext} equals the total rotational energy at a given angular velocity. For baryonic masses exceeding $M_{\text{b,TOV}}$ (i.e., the SMNS scenario), E_{ext} is defined as the difference between the rotational energy at a given spin and that at the point of collapse.

III. RESULTS

The reconstructed equations of state are reported in Figure 1. At the densities about $4n_s$, the quarkyonic model yields results that are consistent with the GP method, though the former has narrower uncertainty ranges. The reduced uncertainties, whose upper boundary approaches the conformal limit at the core densities of massive NSs, render the quarkyonic EOSs generally stiffer in the intermediate density regime. Consequently, the corresponding $R_{1.4}$ ($12.08^{+0.53}_{-0.47}$ km) and $R_{2.0}$ ($12.37^{+0.42}_{-0.43}$ km) are likely higher than that of GP models ($R_{1.4} = 11.94^{+0.52}_{-0.45}$; $R_{2.0} = 11.99^{+0.57}_{-0.47}$). While some difference presents in different approaches in constructing EOSs, their rotational limits are notably similar. As shown in Figure 2, the blue region represents the range of M_{crit} allowed by our EOS ensemble at different spin periods P . For $P \gg 1$ ms, the allowed maximum mass approaches M_{TOV} . It turns out that the massive PSR J0952–0607 [30], if confirmed by the future direct measurement, is consistent with the current knowledge learned from the multi-messenger data. The companion of PSR J0514–4002E has a best-fit gravitational mass of $2.35^{+0.20}_{-0.18}M_{\odot}$ [12], which can be either a neutron star or a low mass black hole because of the lack of other information. The secondary

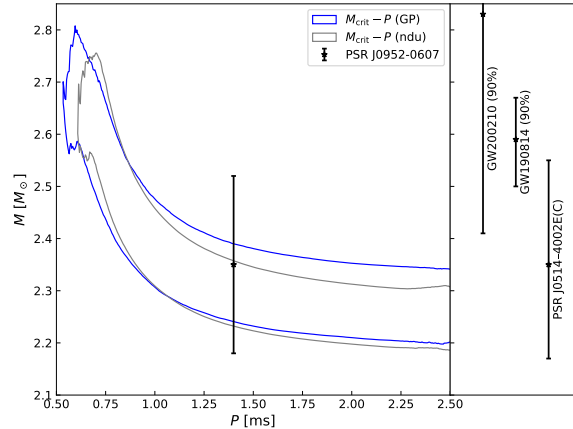


FIG. 2. Critical collapse mass M_{crit} , as a function of rotation period P . The blue and gray curves correspond to the GP and ndu models, respectively. The data of PSR J0952–0607 [30], the companion of PSR J0514–4002E [12] and the secondary stars of GW190814 and GW200210 [14] are shown for comparison.

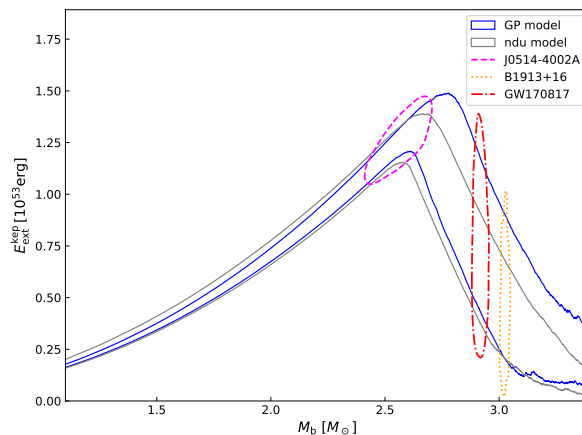


FIG. 3. Extractable rotational energy of NS at mass-shedding limit, $M_{\text{ext}}^{\text{kep}}$, as a function of baryonic mass. The blue and gray curves correspond to the GP and ndu models, respectively. Expected values for J0514–4002A [47], B1913+16 [48], and GW170817 [49] are presented.

star of GW190814 is however too massive to be a neutron star unless the spin is as quick as ≤ 1 ms (see also e.g., Refs. [44, 45]). Even assuming a zero gravitational wave radiation, the strength of the dipole magnetic field should be $\leq 10^9$ Gauss to keep such a quick rotation in a typical merger timescale of ~ 1 Gyr. However, it is widely anticipated that the neutron star born with $P \leq 1$ ms would be accompanied by very strong dipole magnetic field [2, 46]. We thus suggest that the secondary star of GW190814 is most likely a low mass black hole.

For some supramassive neutron stars, the kinetic rotational energy can not be efficiently extracted due to collapse. For this reason, we introduce the term *extractable* rotational energy to reflect the capability of powering the violent explosion by a living neutron star. Figure 3 shows the variation of the extractable rotational energy from NSs rotating at the Keplerian limit, $E_{\text{ext}}^{\text{kep}}$, as a function of baryonic mass. We find that $E_{\text{ext}}^{\text{kep}}$ reaches its maximum at the TOV-limit baryonic mass $M_{\text{b,TOV}}$. The corresponding values are $M_{\text{b,TOV}} = 2.68^{+0.10}_{-0.09} M_{\odot}$, $E_{\text{ext}}^{\text{kep}} = (1.40^{+0.15}_{-0.13}) \times 10^{53}$ erg for the GP model, and $M_{\text{b,TOV}} = 2.63 \pm 0.07 M_{\odot}$, $E_{\text{ext}}^{\text{kep}} = (1.34^{+0.10}_{-0.12}) \times 10^{53}$ erg for the quarkyonic (ndu) model. For baryonic masses below $M_{\text{b,TOV}}$, $E_{\text{ext}}^{\text{kep}}$ increases with mass. However, for supramassive NSs with $M_{\text{b}} > M_{\text{b,TOV}}$, collapse to BHs occurs once sufficient rotational energy is lost, resulting in a decline of $E_{\text{ext}}^{\text{kep}}$ with increasing mass. We also compute

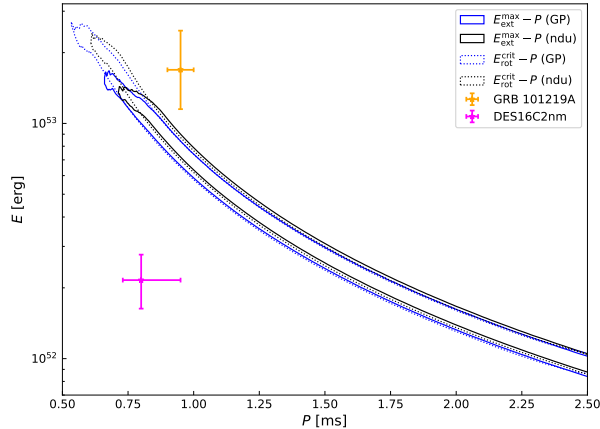


FIG. 4. The solid lines show the maximum extractable rotational energy, $E_{\text{ext}}^{\text{max}}$, for neutron stars with baryonic mass equal to $M_{\text{b,TOV}}$, as a function of rotation period P . The dotted lines represent the maximum rotational energy of neutron stars at a given period. Blue and black curves correspond to the GP and ndu models, respectively. The inferred parameters of DES16C2nm [52] and GRB 101219A [53] are shown for comparison.

the remnant baryonic masses for two Galactic BNS systems (assuming they will merge in the future), as well as for the GW170817 event, and predict their corresponding maximum extractable rotational energies. In these estimates, we assume $0.1 M_{\odot}$ of material remains outside the remnant. J0514-4002A is expected to have $E_{\text{ext}}^{\text{kep}} \approx 1.25 \times 10^{53}$ erg, indicating that the merger remnants of the light double NS systems can indeed serve as one of the sources of the most violent phenomena. However, in heavy systems the extractable energy is significantly reduced due to earlier collapse to black holes. Interestingly, this even happens to GW170817, indicating a quick collapse, in agreement with the argument based on the lack of helium in the spectrum of AT2017gfo [50] (see however Ref. [51]).

Since the rest-mass sequence at $M_{\text{b,TOV}}$ yields the largest extractable rotational energy, we further examine its dependence on spin. In Figure 4, the solid lines present the predicted ranges of the maximum extractable energy, $E_{\text{ext}}^{\text{max}}$ (for $M_{\text{b}} = M_{\text{b,TOV}}$), as a function of spin period P , based on our EOS ensemble. For comparison, we also present the critical kinetic rotational energy of the neutron stars (i.e., the dotted lines). The solid lines overlap with the dotted lines except at the highest spins, for which the neutron stars are supramassive. A specific superluminous supernova, DES16C2nm, at a redshift of 1.998, is highlighted because of the rather short period $P = 0.80^{+0.15}_{-0.07}$ ms as well as the very high rotational kinetic energy of $\approx 3 \times 10^{52}$ erg [52]. This value is already comparable with, though still below, our expected $E_{\text{ext}}^{\text{max}}$ at such a short period, suggesting that DES16C2nm could be among the most energetic superluminous supernovae in recent decades. CDF-S XT2, a $\sim 10^3$ s long X-ray transient with a peak luminosity of $\sim 3 \times 10^{45}$ erg s $^{-1}$, has been attributed to the radiation of the non-collapsing magnetar formed in a double neutron star merger [54]. Evidently, unless the X-ray emission efficiency is as low as $\sim 10^{-5}$ or most of the energy has been radiated in gravitational wave [55, 56], the magnetar interpretation has a serious missing energy problem. Another direct application of our Figure 4 is on the magnetar interpretation of the X-ray plateau of GRB 101219A, which requires a rotation period of 0.95 ms and the energy of 1.7×10^{53} erg [53], significantly exceeding our predicted $E_{\text{ext}}^{\text{max}}(P = 0.95 \text{ ms})$.

IV. SUMMARY

In this work, we explored the maximum mass, rotational energy and extractable energy of rapidly rotating neutron stars, using a range of equations of state constrained by the latest multimessenger data. We computed sequences of uniformly rotating neutron stars, extending to the mass-shedding limit, and examined how the critical collapse mass, total rotational energy, and extractable energy vary with spin period. We then compared the constrained ranges of the critical collapse mass with observed data, such as the measured masses of PSR J0952-0607 and the companion of PSR J0514-4002E. It turns out that both objects may be supra-massive neutron stars, stabilized by rapid rotation. But for the secondary star of GW190814, it is too massive and a neutron star is only possible with an almost mass-shedding rotation as well as an extremely low dipole magnetic field. As for the energy budget, though many superluminous supernovae have been detected and the magnetar model has been adopted to fit the data, the

inferred highest rotational energy is $\sim 3 \times 10^{52}$ erg for a $P \sim 0.8$ ms [52], which well satisfies our bound and likely indicates a gravitational mass considerably below $M_{\text{kep}}^{\text{crit}}$. However, for GRB 101219A, the claimed $P \sim 0.95$ ms with a rotational energy of $\sim 1.7 \times 10^{53}$ erg [53] is in tension with our $E_{\text{ext}}^{\text{max}}$ limit (see Figure 4). We also caution that the interpretation of short GRB data using the merger-formed magnetar model often suffers from a significant energy deficit problem, unless most of the angular momentum, and thus the rotational energy, of the nascent remnant is efficiently carried away by gravitational waves [55]. Our final remark is that the remnants formed in the mergers of the lightest neutron star binaries are most likely supramassive or even stable, and the energy reservoir represented by $E_{\text{ext}}^{\text{max}}$ will be sufficient to produce extremely luminous counterparts and accelerate a large amount of ultra-high energy cosmic rays. The detection of such violent events in the future would further strength our conclusion.

ACKNOWLEDGMENTS

This work is supported by the National Natural Science Foundation of China under Grants No. 12233011 and No. 12303056, the Project for Special Research Assistant and the Project for Young Scientists in Basic Research (No. YSBR-088) of the Chinese Academy of Sciences, the General Fund (No. 2023M733736) of the China Postdoctoral Science Foundation (CPSF), and the Postdoctoral Fellowship Program of CPSF (GZB20230839, GZC20241915).

-
- [1] V. V. Usov, *Nature* **357**, 472 (1992).
[2] R. C. Duncan and C. Thompson, *ApJL* **392**, L9 (1992).
[3] W. Kluźniak and M. Ruderman, *ApJL* **505**, L113 (1998), arXiv:astro-ph/9712320 [astro-ph].
[4] Z. G. Dai and T. Lu, *A&A* **333**, L87 (1998), arXiv:astro-ph/9810402 [astro-ph].
[5] B. Zhang and P. Mészáros, *ApJL* **552**, L35 (2001), arXiv:astro-ph/0011133 [astro-ph].
[6] W.-H. Gao and Y.-Z. Fan, *Chinese J Astron Astrophys* **6**, 513 (2006), arXiv:astro-ph/0512646 [astro-ph].
[7] D. Kasen and L. Bildsten, *ApJ* **717**, 245 (2010), arXiv:0911.0680 [astro-ph.HE].
[8] S. E. Woosley, *ApJL* **719**, L204 (2010), arXiv:0911.0698 [astro-ph.HE].
[9] Y. Sekiguchi, K. Kiuchi, K. Kyutoku, and M. Shibata, *Phys Rev Lett* **107**, 051102 (2011), arXiv:1105.2125 [gr-qc].
[10] L. Baiotti and L. Rezzolla, *Reports on Progress in Physics* **80**, 096901 (2017), arXiv:1607.03540 [gr-qc].
[11] J. Greiner, P. A. Mazzali, D. A. Kann, *et al.*, *Nature* **523**, 189 (2015), arXiv:1509.03279 [astro-ph.HE].
[12] E. D. Barr, A. Dutta, P. C. C. Freire, M. Cadelano, T. Gautam, M. Kramer, C. Pallanca, S. M. Ransom, A. Ridolfi, B. W. Stappers, T. M. Tauris, V. Venkatraman Krishnan, N. Wex, M. Bailes, J. Behrend, S. Buchner, M. Burgay, W. Chen, D. J. Champion, C. H. R. Chen, A. Corongiu, M. Geyer, Y. P. Men, P. V. Padmanabh, and A. Possenti, *Science* **383**, 275 (2024), arXiv:2401.09872 [astro-ph.HE].
[13] R. Abbott, T. D. Abbott, S. Abraham, *et al.*, *ApJL* **896**, L44 (2020), arXiv:2006.12611 [astro-ph.HE].
[14] R. Abbott, T. D. Abbott, F. Acernese, *et al.*, *Physical Review X* **13**, 041039 (2023), arXiv:2111.03606 [gr-qc].
[15] D. Choudhury, T. Salmi, S. Vinciguerra, T. E. Riley, Y. Kini, A. L. Watts, B. Dorsman, S. Bogdanov, S. Guillot, P. S. Ray, D. J. Reardon, R. A. Remillard, A. V. Bilous, D. Huppenkothen, J. M. Lattimer, N. Rutherford, Z. Arzoumanian, K. C. Gendreau, S. M. Morsink, and W. C. G. Ho, *ApJL* **971**, L20 (2024), arXiv:2407.06789 [astro-ph.HE].
[16] S. Vinciguerra, T. Salmi, A. L. Watts, D. Choudhury, T. E. Riley, P. S. Ray, S. Bogdanov, Y. Kini, S. Guillot, D. Chakrabarty, W. C. G. Ho, D. Huppenkothen, S. M. Morsink, Z. Wadiasingh, and M. T. Wolff, *ApJ* **961**, 62 (2024), arXiv:2308.09469 [astro-ph.HE].
[17] T. Salmi, D. Choudhury, Y. Kini, T. E. Riley, S. Vinciguerra, A. L. Watts, M. T. Wolff, Z. Arzoumanian, S. Bogdanov, D. Chakrabarty, K. Gendreau, S. Guillot, W. C. G. Ho, D. Huppenkothen, R. M. Ludlam, S. M. Morsink, and P. S. Ray, *ApJ* **974**, 294 (2024), arXiv:2406.14466 [astro-ph.HE].
[18] A. J. Dittmann, M. C. Miller, F. K. Lamb, I. M. Holt, C. Chirenti, M. T. Wolff, S. Bogdanov, S. Guillot, W. C. G. Ho, S. M. Morsink, Z. Arzoumanian, and K. C. Gendreau, *ApJ* **974**, 295 (2024), arXiv:2406.14467 [astro-ph.HE].
[19] B. P. Abbott, R. Abbott, T. D. Abbott, *et al.*, *Phys Rev Lett* **121**, 161101 (2018), arXiv:1805.11581 [gr-qc].
[20] B. P. Abbott, R. Abbott, T. D. Abbott, *et al.*, *Physical Review X* **9**, 011001 (2019), arXiv:1805.11579 [gr-qc].
[21] O. Komoltsev and A. Kurkela, *Phys Rev Lett* **128**, 202701 (2022), arXiv:2111.05350 [nucl-th].
[22] T. Gorda, A. Kurkela, R. Paatelainen, S. Säppi, and A. Vuorinen, *Phys Rev Lett* **127**, 162003 (2021), arXiv:2103.05658 [hep-ph].
[23] T. Gorda, O. Komoltsev, and A. Kurkela, *ApJ* **950**, 107 (2023), arXiv:2204.11877 [nucl-th].
[24] M.-Z. Han, Y.-J. Huang, S.-P. Tang, and Y.-Z. Fan, *Science Bulletin* **68**, 913 (2023), arXiv:2207.13613 [astro-ph.HE].
[25] J. Alsing, H. O. Silva, and E. Berti, *MNRAS* **478**, 1377 (2018), arXiv:1709.07889 [astro-ph.HE].
[26] D.-S. Shao, S.-P. Tang, J.-L. Jiang, and Y.-Z. Fan, *Phys Rev D* **102**, 063006 (2020), arXiv:2009.04275 [astro-ph.HE].
[27] Y.-Z. Fan, M.-Z. Han, J.-L. Jiang, D.-S. Shao, and S.-P. Tang, *Phys Rev D* **109**, 043052 (2024), arXiv:2309.12644 [astro-ph.HE].
[28] S.-P. Tang, Y.-J. Huang, M.-Z. Han, and Y.-Z. Fan, *ApJ* **974**, 244 (2024), arXiv:2404.09563 [astro-ph.HE].
[29] B. Biswas and S. Rosswog, *arXiv e-prints*, arXiv:2408.15192 (2024), arXiv:2408.15192 [astro-ph.HE].

- [30] R. W. Romani, D. Kandel, A. V. Filippenko, T. G. Brink, and W. Zheng, *ApJL* **934**, L17 (2022), arXiv:2207.05124 [astro-ph.HE].
- [31] N. Stergioulas and J. L. Friedman, *ApJ* **444**, 306 (1995), arXiv:astro-ph/9411032 [astro-ph].
- [32] C. Breu and L. Rezzolla, *MNRAS* **459**, 646 (2016), arXiv:1601.06083 [gr-qc].
- [33] J.-L. Jiang, C. Ecker, and L. Rezzolla, *ApJ* **949**, 11 (2023), arXiv:2211.00018 [gr-qc].
- [34] P. Landry and R. Essick, *Phys Rev D* **99**, 084049 (2019), arXiv:1811.12529 [gr-qc].
- [35] R. Essick, P. Landry, and D. E. Holz, *Phys Rev D* **101**, 063007 (2020), arXiv:1910.09740 [astro-ph.HE].
- [36] P. Landry, R. Essick, and K. Chatziioannou, *Phys Rev D* **101**, 123007 (2020), arXiv:2003.04880 [astro-ph.HE].
- [37] S.-P. Tang, M.-Z. Han, Y.-J. Huang, Y.-Z. Fan, and D.-M. Wei, *Phys Rev D* **109**, 083037 (2024), arXiv:2311.13805 [astro-ph.HE].
- [38] L. McLerran and S. Reddy, *Phys Rev Lett* **122**, 122701 (2019), arXiv:1811.12503 [nucl-th].
- [39] Y. Fujimoto, T. Kojo, and L. D. McLerran, *Phys Rev Lett* **132**, 112701 (2024), arXiv:2306.04304 [nucl-th].
- [40] T. Zhao and J. M. Lattimer, *Phys Rev D* **102**, 023021 (2020), arXiv:2004.08293 [astro-ph.HE].
- [41] C. Drischler, P. G. Giuliani, S. Bezoui, J. Piekarewicz, and F. Viens, *Phys Rev C* **110**, 044320 (2024), arXiv:2405.02748 [nucl-th].
- [42] F. Douchin and P. Haensel, *A&A* **380**, 151 (2001), arXiv:astro-ph/0111092 [astro-ph].
- [43] C.-N. Luo, S.-P. Tang, M.-Z. Han, J.-L. Jiang, W.-H. Gao, and D.-M. Wei, *ApJ* **966**, 98 (2024), arXiv:2403.14105 [astro-ph.HE].
- [44] E. R. Most, L. J. Papenfort, L. R. Weih, and L. Rezzolla, *MNRAS* **499**, L82 (2020), arXiv:2006.14601 [astro-ph.HE].
- [45] B.-A. Li, B.-J. Cai, W.-J. Xie, and N.-B. Zhang, *Universe* **7**, 182 (2021), arXiv:2105.04629 [nucl-th].
- [46] D. J. Price and S. Rosswog, *Science* **312**, 719 (2006), arXiv:astro-ph/0603845 [astro-ph].
- [47] A. Ridolfi, P. C. C. Freire, Y. Gupta, and S. M. Ransom, *MNRAS* **490**, 3860 (2019), arXiv:1909.06163 [astro-ph.HE].
- [48] J. M. Weisberg, D. J. Nice, and J. H. Taylor, *ApJ* **722**, 1030 (2010), arXiv:1011.0718 [astro-ph.GA].
- [49] B. P. Abbott, R. Abbott, T. D. Abbott, S. Abraham, F. Acernese, K. Ackley, C. Adams, *et al.*, *Physical Review X* **9**, 031040 (2019), arXiv:1811.12907 [astro-ph.HE].
- [50] A. Snuppen, O. Just, A. Bauswein, R. Damgaard, D. Watson, L. J. Shingles, C. E. Collins, S. A. Sim, Z. Xiong, G. Martinez-Pinedo, T. Soutanis, and V. Vijayan, *arXiv e-prints*, arXiv:2411.03427 (2024), arXiv:2411.03427 [astro-ph.HE].
- [51] Y.-W. Yu, L.-D. Liu, and Z.-G. Dai, *ApJ* **861**, 114 (2018), arXiv:1711.01898 [astro-ph.HE].
- [52] B. Hsu, G. Hosseinzadeh, and E. Berger, *ApJ* **921**, 180 (2021), arXiv:2104.09639 [astro-ph.HE].
- [53] A. Rowlinson, P. T. O'Brien, B. D. Metzger, N. R. Tanvir, and A. J. Levan, *MNRAS* **430**, 1061 (2013), arXiv:1301.0629 [astro-ph.HE].
- [54] Y. Q. Xue, X. C. Zheng, Y. Li, W. N. Brandt, B. Zhang, B. Luo, B. B. Zhang, F. E. Bauer, H. Sun, B. D. Lehmer, X. F. Wu, G. Yang, X. Kong, J. Y. Li, M. Y. Sun, J. X. Wang, and F. Vito, *Nature* **568**, 198 (2019), arXiv:1904.05368 [astro-ph.HE].
- [55] Y.-Z. Fan, X.-F. Wu, and D.-M. Wei, *Phys Rev D* **88**, 067304 (2013), arXiv:1302.3328 [astro-ph.HE].
- [56] H.-J. Lü, H.-M. Zhang, S.-Q. Zhong, S.-J. Hou, H. Sun, J. Rice, and E.-W. Liang, *ApJ* **835**, 181 (2017), arXiv:1612.05691 [astro-ph.HE].
- [57] I. Tews, J. M. Lattimer, A. Ohnishi, and E. E. Kolomeitsev, *ApJ* **848**, 105 (2017), arXiv:1611.07133 [nucl-th].
- [58] C. Drischler, R. J. Furnstahl, J. A. Melendez, and D. R. Phillips, *Phys Rev Lett* **125**, 202702 (2020), arXiv:2004.07232 [nucl-th].
- [59] P. T. H. Pang, L. Sivertsen, R. Somasundaram, T. Dietrich, S. Sen, I. Tews, M. W. Coughlin, and C. Van Den Broeck, *Phys Rev C* **109**, 025807 (2024), arXiv:2308.15067 [nucl-th].

APPENDIX

In this appendix, we provide additional details regarding the posterior distributions of the quarkyonic model parameters, a comparison of the bulk properties of neutron stars (NSs) derived from the Gaussian process (GP) and quarkyonic models, and the reconstructed mass-radius relations. These analyses complement the main text and offer further insights into the equations of state (EOSs) constrained by recent multi-messenger NS observations and theoretical advancements. Using these constrained EOSs, we subsequently determine the rotational properties of neutron stars. Finally, we explore universal relations for the critical rotational energy derived from posterior samples of the GP model.

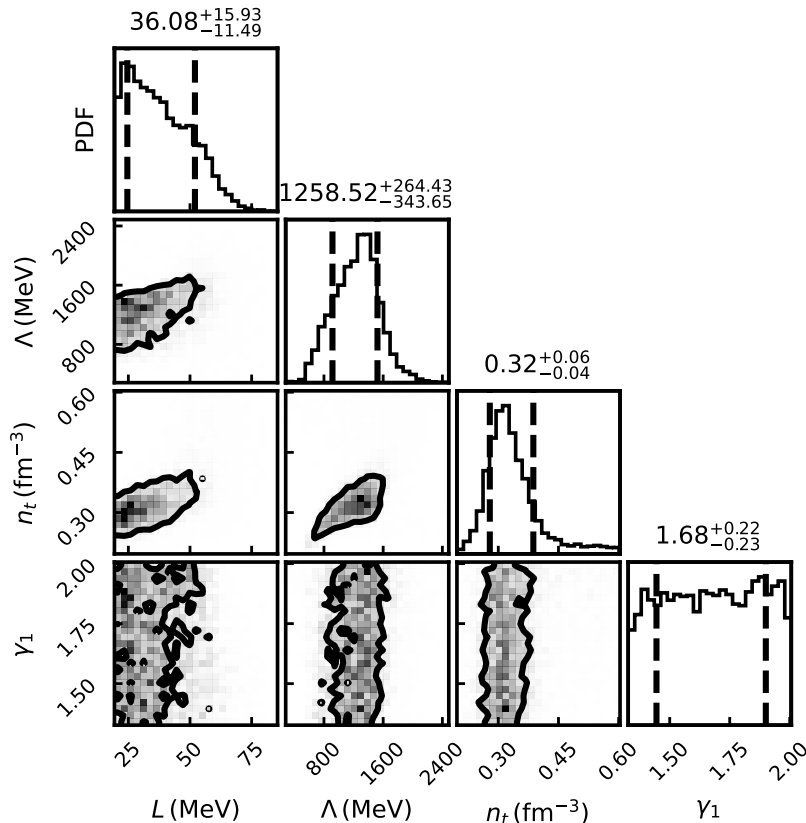


FIG. 5. Posterior distributions of key parameters from the quarkyonic model, including the slope of symmetry energy L , the parameter Λ , the threshold density n_t , and the potential parameter γ_1 . The values and their 68.3% credible intervals are shown for each parameter.

Figure 5 displays the posterior distributions of key parameters from the quarkyonic model, including the slope of the symmetry energy L , the parameter Λ , the threshold density n_t , and the potential parameter γ_1 . Notably, the slope of the symmetry energy L is concentrated at the lower edge, with a value of $36.08^{+15.93}_{-11.49}$ MeV, consistent with constraints from nuclear experiments [57, 58]. Additionally, the threshold density n_t is well-constrained to $0.32^{+0.06}_{-0.04}$ fm^{-3} , indicating a rapid stiffening that occurs at approximately twice the nuclear saturation density. Figure 6 compares the bulk properties of NSs derived from the GP and quarkyonic models, including the maximum mass (M_{TOV}) and corresponding radius (R_{TOV}) of a nonrotating NS, the radius ($R_{1.4}$) and tidal deformability ($\Lambda_{1.4}$) of a canonical $1.4 M_{\odot}$ NS, the radius of a $1.4 M_{\odot}$ NS ($R_{2.0}$), and the difference between $R_{1.4}$ and $R_{2.0}$. Both models yield consistent results, particularly for M_{TOV} , with the quarkyonic model tending to favor slightly larger radii. Figure 7 shows the mass-radius relations for neutron stars reconstructed using the GP and quarkyonic models, along with the corresponding observational data for various neutron stars and gravitational wave events. The contours represent the 68.3% credible regions for both models, with blue denoting the GP model and gray denoting the quarkyonic model. The mass-radius relations predicted by the two models are broadly similar, with the quarkyonic model suggesting slightly larger radii across the entire mass range. However, this is still much smaller than the results found in Ref. [59] (with $R_{1.4} \sim 13.44$ km). This discrepancy may arise because the nondynamical quarkyonic model refined by Zhao

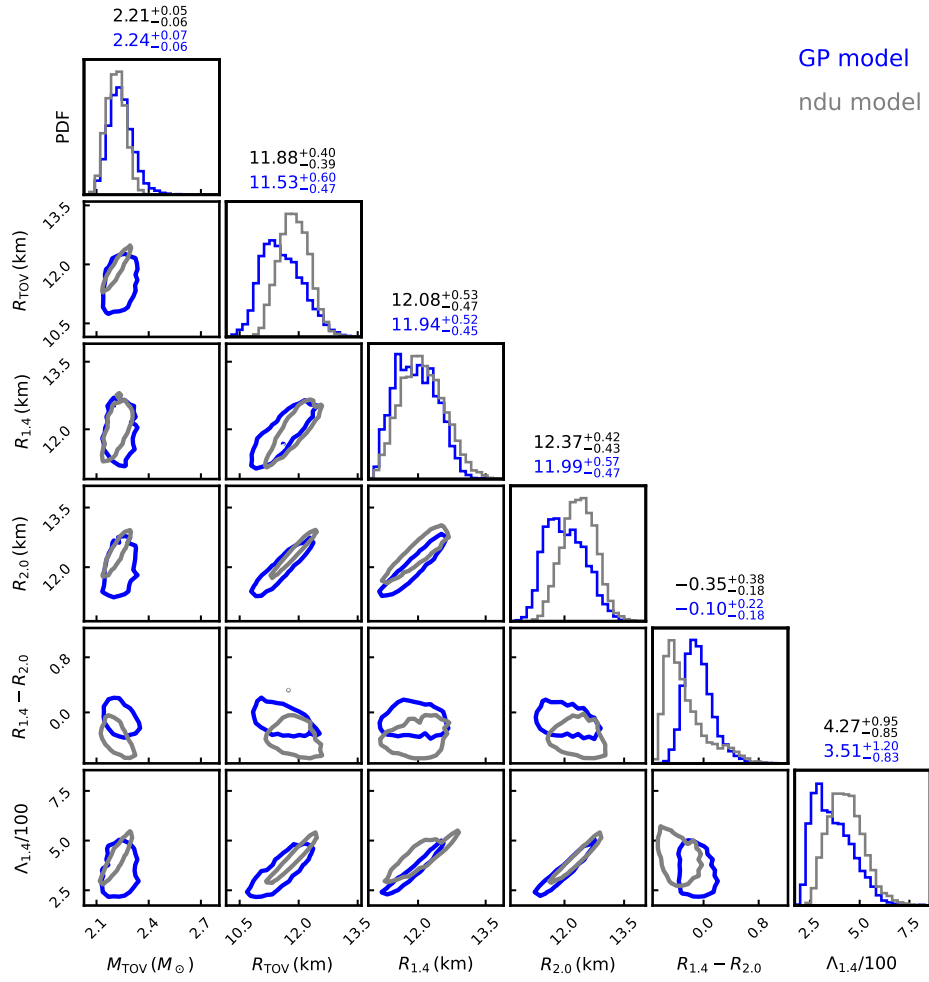


FIG. 6. Comparison of the bulk properties of NSs derived from the GP (blue) and quarkyonic (gray) models. The corresponding 68.3% credible intervals are indicated above the diagonal subplots.

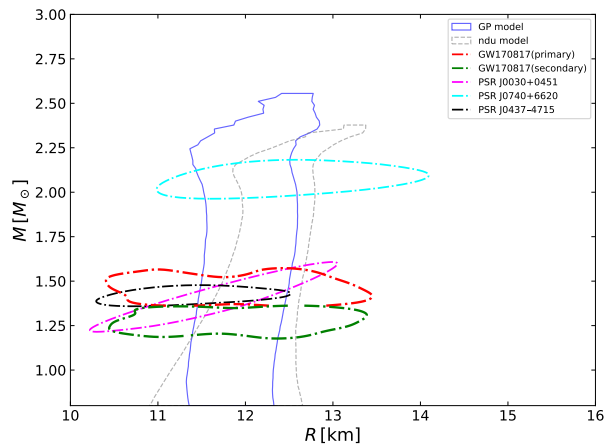


FIG. 7. The 68.3% credible mass-radius intervals reconstructed using the GP (blue) and quarkyonic (gray) models. The mass-radius data for PSR J0030+0451, PSR J0740+6620, PSR J0437-4715, and the components of the GW170817 event are shown for comparison.

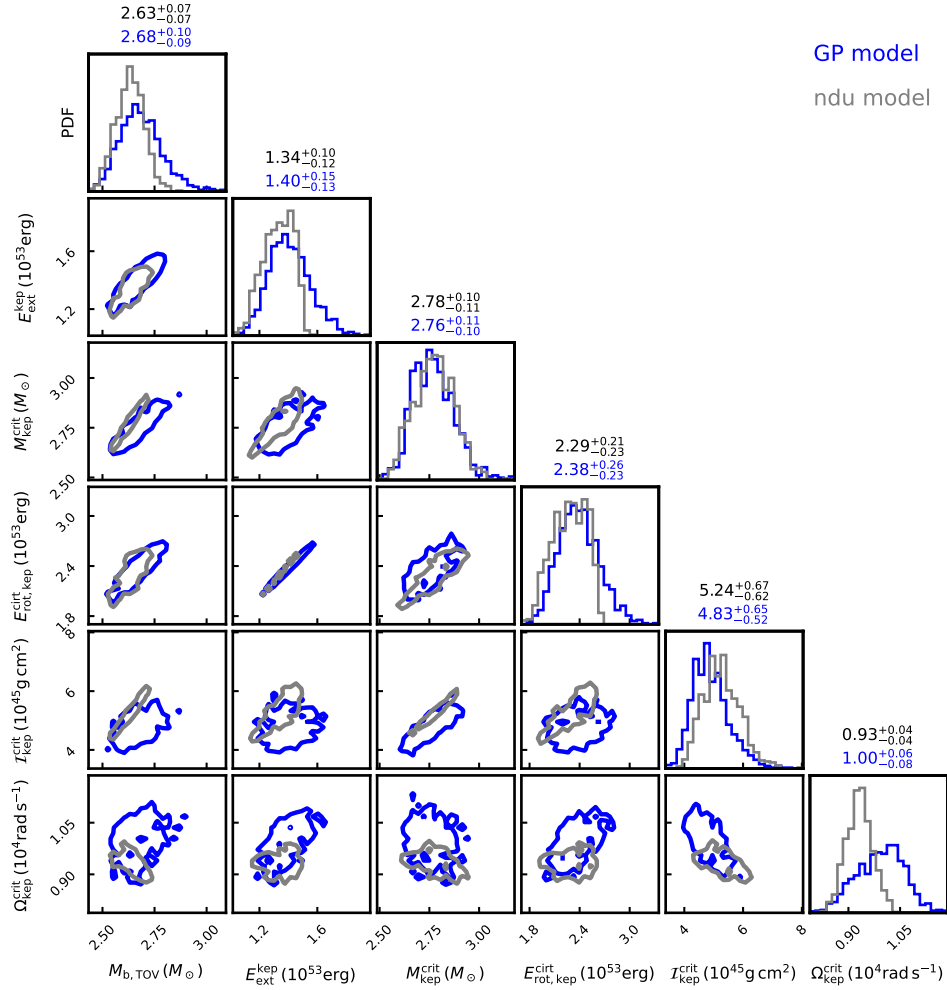


FIG. 8. Corner plot showing joint posterior distributions of the maximum baryonic mass of nonrotating neutron stars $M_{b, \text{TOV}}$, the corresponding extractable energy at the Keplerian limit $E_{\text{ext}}^{\text{kep}}$, the critical gravitational mass at the Keplerian limit $M_{\text{kep}}^{\text{crit}}$, the corresponding rotational energy $E_{\text{rot, kep}}^{\text{crit}}$, moment of inertia $I_{\text{kep}}^{\text{crit}}$, and angular velocity $\Omega_{\text{kep}}^{\text{crit}}$. Values displayed above the diagonal panels indicate the 68% credible intervals for each parameter.

and Lattimer [40] includes beta equilibrium, and the adoption of the ndu model, though simplified, provides a more accurate representation, leading to better alignment with the observed NS radii.

Figure 8 summarizes the key rotational properties of neutron stars. For a star with baryonic mass equal to the nonrotating maximum ($M_{b, \text{TOV}}$), the extractable energy at the Keplerian limit $E_{\text{ext}}^{\text{kep}}$ is estimated to be $1.40^{+0.15}_{-0.13} \times 10^{53}$ erg (GP) and $1.34^{+0.10}_{-0.12} \times 10^{53}$ erg (ndu). The critical gravitational mass at the Keplerian limit $M_{\text{kep}}^{\text{crit}}$ is similar between models, with $2.76^{+0.10}_{-0.10} M_{\odot}$ (GP) and $2.78^{+0.10}_{-0.11} M_{\odot}$ (ndu). The corresponding critical rotational energy $E_{\text{rot, kep}}^{\text{crit}}$ is $2.38^{+0.26}_{-0.23} \times 10^{53}$ erg (GP) and $2.29^{+0.21}_{-0.23} \times 10^{53}$ erg (ndu). The moment of inertia $I_{\text{kep}}^{\text{crit}}$ differs slightly, with GP predicting $4.83^{+0.65}_{-0.52} \times 10^{45}$ g cm² and ndu $5.24^{+0.67}_{-0.62} \times 10^{45}$ g cm². Finally, the angular velocity $\Omega_{\text{kep}}^{\text{crit}}$ at the Keplerian limit is higher for the GP model, $1.00^{+0.06}_{-0.08} \times 10^4$ rad s⁻¹, compared to $0.93^{+0.04}_{-0.04} \times 10^4$ rad s⁻¹ for the ndu model.

We also update some universal relations regarding the total rotational energy, E_{rot} . As shown in Figure 9, the normalized critical rotational energy, $\bar{E} = E_{\text{rot, j}}^{\text{crit}} / E_{\text{rot, kep}}^{\text{crit}}$ (where $E_{\text{rot, kep}}^{\text{crit}}$ is the critical rotational energy at the Kepler limit), exhibits an excellent correlation with the normalized dimensionless angular momentum, $j_{\text{crit}} / j_{\text{crit, kep}}$. The solid black curve represents a polynomial fit, $y = 0.51x^2 + 0.49x^3$, and the lower panel displays the fractional residual. The scatter of points reflects the uncertainty across our EOS ensemble, illustrating that despite these uncertainties, the normalized critical rotational energy follows a smooth, predictable trend as the star's spin approaches the mass-shedding limit. We further examine the correlation between the rotational energy at the mass-shedding limit, $E_{\text{rot, kep}}$, and the corresponding stellar mass, m_{kep} . Figure 10 displays this relationship: the horizontal axis represents m_{kep} (in M_{\odot}), while the vertical axis shows $E_{\text{rot, kep}}$ in units of 10^{53} erg. A polynomial fit, $y = 0.07x^3 + 0.13x^2 - 0.06x$,

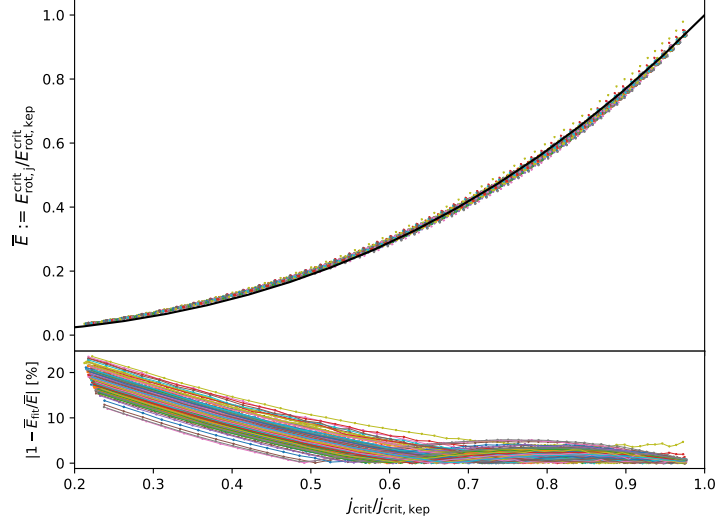


FIG. 9. Normalized critical rotational energy, $\bar{E} = E_{\text{rot},j}^{\text{crit}}/E_{\text{rot,kep}}^{\text{crit}}$, plotted as a function of the normalized spin parameter, $j_{\text{crit}}/j_{\text{crit,kep}}$. Colored points in the top panel represent the rotational properties of neutron stars computed from posterior samples of our EOS ensemble, while the solid black curve shows a polynomial fit to the data. The bottom panel displays the fractional residual, $|1 - \bar{E}_{\text{fit}}/\bar{E}|$, demonstrating that the polynomial approximation reproduces the data within a few percent.

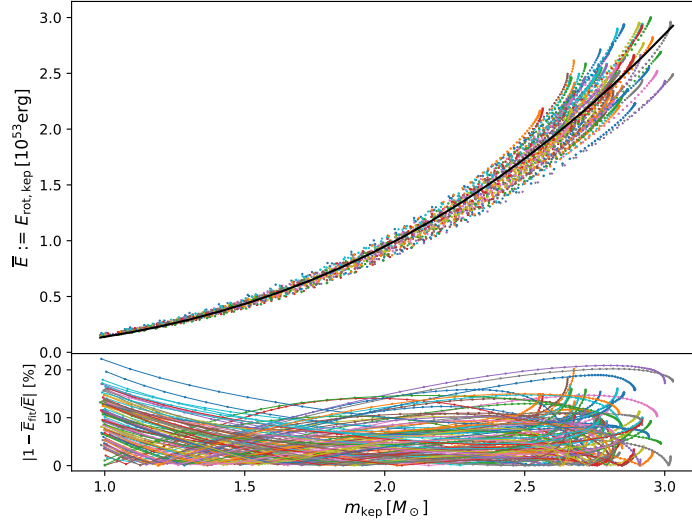


FIG. 10. Rotational energy at the Kepler limit, $E_{\text{rot,kep}}$ (in 10^{53} erg), as a function of the neutron star mass m_{kep} . The black line is a polynomial fit and the bottom panel displays the fractional residual.

captures the trend well, with the bottom panel depicting the relative residual. This systematic behavior indicates that although different EOSs produce variations in the maximum mass at the mass-shedding limit, the underlying functional dependence between $E_{\text{rot,kep}}$ and m_{kep} remains robust. These universal relations are valuable for estimating the rotational energy reservoir of a supramassive neutron star formed after a binary neutron star merger, even without precise knowledge of neutron star EOS.